SYNTHESIS AND CHARACTERIZATION OF **LI- AND NA-ION BATTERY MATERIALS**

Biological and Chemical Engineering
Technical Report BCE-TR-10

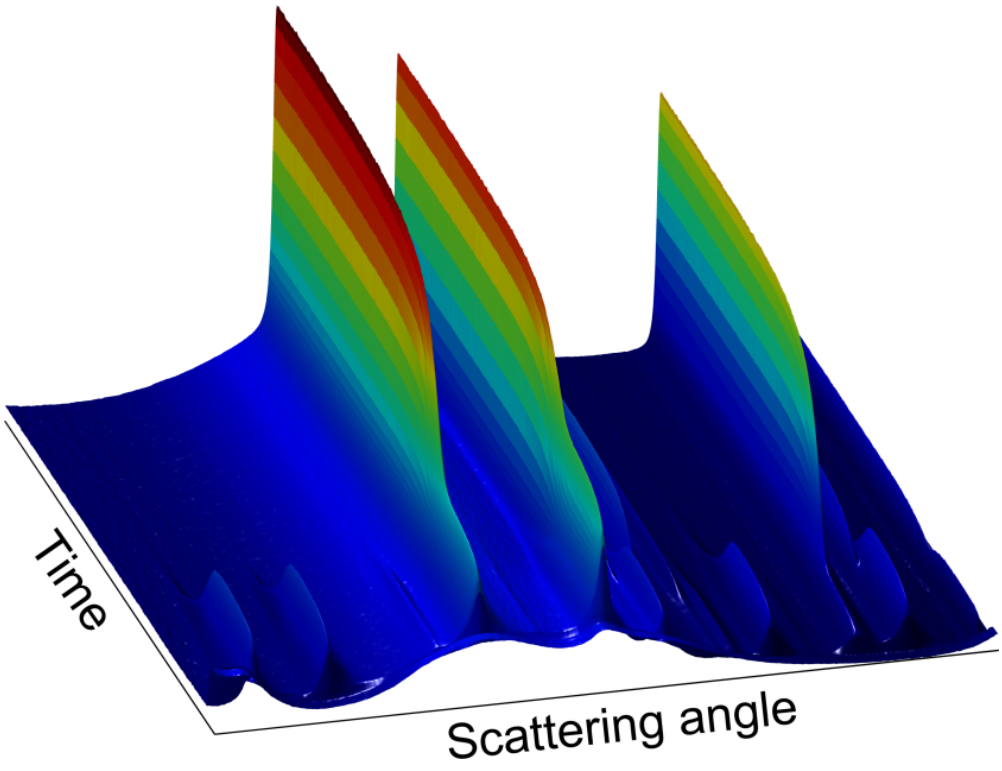

AARHUS
UNIVERSITY
DEPARTMENT OF ENGINEERING

DATA SHEET

Title: Synthesis and characterization of Li- and Na-ion battery materials
Subtitle: Biological and Chemical Engineering
Series title and no.: Technical report BCE-TR-10

Author: Steinar Birgisson, Department of Engineering – Biological and Chemical Engineering, Aarhus University

Internet version: The report is available in electronic format (pdf) at the Department of Engineering website http://www.eng.au.dk.

Publisher: Aarhus University©
URL: http://www.eng.au.dk

Year of publication: 2015 Pages: 30
Editing completed: March 2015

Abstract: This report contains description of my first half of PhD research along with a short introduction to the field of research and a brief description about the research plan for the remainder of my PhD studies. The report presents *in situ* results from hydrothermal synthesis of spinel type $LiMn_2O_4$ and various structural phases of MnO_2. The hydrothermal synthesis of spinel type $LiMn_2O_4$ was studied using *in situ* powder X-ray diffraction to see the effect of reaction time, temperature, LiOH concentration and different reducing agent on the crystalline products of the synthesis. Hydrothermal formation of α-, β-, γ- and δ-MnO_2 were studied using *in situ* powder X-ray diffraction and *in situ* pair distribution function to understand reaction mechanisms leading to the various MnO_2 phases.

Keywords: Powder X-ray diffraction, Pair distribution function, Li-ion batteries. Na-ion batteries, Material synthesis, Nanotechnology and nanoscience, Particles

Supervisor:
Bo Brummerstedt Iversen, Professor, dr. scient. et. techn.
Co-supervisor:
Søren Dahl, PhD

Financial support: This work has been supported by funds from the Danish National Research Foundation (Center for Materials Crystallography), Haldor Topsoe A/S and DANSCATT.

Please cite as: Steinar Birgisson, 2015. Synthesis and characterization of Li- and Na-ion battery materials. Department of Engineering, Aarhus University. Denmark. 30 pp. - Technical report BCE -TR-10

Cover image: Steinar Birgisson

ISSN: 2245-5817

SYNTHESIS AND CHARACTERIZATION OF **LI- AND NA-ION BATTERY MATERIALS**

Steinar Birgisson
Aarhus University, Department of Engineering

Abstract

This report contains description of my first half of PhD research along with a short introduction to the field of research and a brief description about the research plan for the remainder of my PhD studies. The report presents *in situ* results from hydrothermal synthesis of spinel type $LiMn_2O_4$ and various structural phases of MnO_2. The hydrothermal synthesis of spinel type $LiMn_2O_4$ was studied using *in situ* powder X-ray diffraction to see the effect of reaction time, temperature, LiOH concentration and different reducing agent on the crystalline products of the synthesis. Hydrothermal formation of α-, β-, γ- and δ-MnO_2 were studied using *in situ* powder X-ray diffraction and *in situ* pair distribution function to understand reaction mechanisms leading to the various MnO_2 phases.

Contents

Acknowledgements

I would especially like to thank my supervisor Professor Bo Brummerstedt Iversen for the great collaboration during the last two years. I would also like to thank my co-supervisor Søren Dahl for believing in me and making my research possible. I would also like to thank the in situ dream team; Mogens Christensen, Kirsten M. Ørnsbjerg Jensen, Christoffer Tyrsted, Espen Drath Bøjesen, Dipankar Saha, Peter Nørby, Cecilia Granados Miralles, Henrik Lyder Andersen and Gilles Philippot, for great moral and invaluable support during beam times and data analysis. Furthermore, a big thanks goes out to the battery group; Yanbin Shen, Martin Søndergaard, Kirsten M. Ørnsbjerg Jensen, Troels L. Christiansen and Mette Østergaard Filsø, for all the collaboration and helping me learn all I know about batteries. Last but not least I would like to thank the international office (same geographic location as the former girls office) and the whole inorganic department for creating a work place I look forward to coming in to in the morning and lucky to be a part of in the evening. Espen Drath Bøjesen and Hazel Reardon are thanked for the proof reading and fruitful discussions about the results presented in this report. Of course this section cannot pass without me expressing my deepest gratitude to my wife, Snæfríður Dröfn Björgvinsdóttir, and my two beautiful daughters, Katrín and Margrét. Without their love and support I would not be where I am today.

This work has been supported by funds from the Danish National Research Foundation (Center for Materials Crystallography), Haldor Topsoe A/S and DANSCATT.

Motivation

Since the introduction of the first commercial Lithium ion battery (LIB) by Sony in 1991[1] the technology has been widely accepted due to its high energy density and good cyclability. It has been very successful for powering portable electronics and it is the dominating battery type in that market. LIBs have been considered a possible replacement for fossil fuels as an energy carrier for transportation. Another emerging application is large scale energy storage in power grids to accommodate for intermittent power production from renewable sources such as solar and wind power.[2] The emergence of new applications brings challenges to the field of battery research, e.g., the need for higher energy density, higher rate capabilities, improved safety and lower cost.[3] Sodium ion secondary batteries (SIBs) are now being considered as an alternative to LIBs because sodium is considerably more abundant than lithium rendering SIBs a cheaper alternative. Sodium ions have a higher atomic weight, compared to lithium ions, making the gravimetric energy density of SIBs lower than for LIBs. However, this does not pose a problem for stationary large scale grid energy storage since minimizing the overall mass of the batteries is less critical.[4]

At the heart of LIBs and SIBs are the electrode materials. The electrode materials play a large role in determining numerous properties of the batteries including; specific capacity, potential, coulombic efficiency and rate capability. These properties are mainly determined by the crystal structure of the material and partly by other (micro)-structural properties, e.g. crystallite size, particle size, unit cell size and defects in the crystal structure. Therefore it is essential to be able to control (micro)-structural properties of electrode materials, e.g. through synthesis, in order to prepare the best possible battery for a specific application.

This PhD project aims at synthesizing and characterizing different inorganic materials for use as electrode materials in LIBs and SIBs. The main focus during my first 2 years of PhD research has

been on *in situ* hydrothermal synthesis of $LiMn_2O_4$ and MnO_2, which are well known cathode materials for LIBs. Using an experimental setup developed by our research group (see section 1.3.3), a rare and unique opportunity to study the structural and microstructural properties of the materials being synthesized while the reaction is happening is obtained. Characterization of the *in situ* solvothermal synthesis was conducted by PXRD and PDF. This approach provides the opportunity to understand fundamental formation mechanism(s) and reaction kinetics. Additionally, from a practical perspective, it also gives insight in to how the solvothermal synthesis may be controlled and optimized to obtain materials with desirable properties. The remaining 2 years of my PhD research will focus on synthesis and characterization of layered Na_xMO_2 materials (M, transition metal) which can be used as cathode materials in SIBs. These materials will be characterized in order to understand the connection between structural and microstructural properties with battery performance. Moreover, I will investigate the structural evolution upon battery cycling by *in operando* characterization. *In operando* characterization of working half cells, using experimental setup developed by our research group (see section 3.1.2.5), allows us to follow structural changes while the battery is being charged and discharged. This method will enable a better understanding of how structure and function are correlated in the assemblies produced in this work.

1 Introduction

Li- and Na-ion batteries work on the so-called rocking chair mechanism. The redox process involved in this mechanism depends upon extraction of alkali ions from one electrode and insertion into the other, i.e., rocking the ions back and forth. The alkali ion is usually part of the cathode material, typically a metal oxide, e.g. $LiCoO_2$. The battery is thus assembled in a discharged state. Upon charging, electrons are removed from the cathode and inserted into the anode, e.g. graphite, by an external power source. This consequently oxidizes the metal ion in the cathode material and reduces the redox center on the anode side. In order to retain charge balance the alkali ion simultaneously de-intercalates from the cathode material and intercalates to the anode material. The charging process creates a potential difference depending on the chemical potential difference between the redox couples on the anode and cathode side. During the discharge, chemical equilibrium is restored by letting electrons flow through an external circuit accompanied by de-intercalation/intercalation of the alkali ion.[5]

1.1 Electrode materials

The most important components of every battery cell are the negative and positive electrodes. The electrode materials set the upper limit to the amount of energy that can be stored in the cell. Additionally, the electrode materials often contribute significantly to other battery properties, including rate capabilities and impedance of the cell. The capability of an electrode material to store energy is most conveniently measured by the specific energy density (volumetric or gravimetric) of the material. It is defined as the product of the electrochemical potential of the material and the specific capacity, i.e. the amount of electrons that can be extracted from the material per mass or volume. While the redox couple plays the principal role in determining the electrochemical potential it can be affected by the crystal structure of the electrode material. The crystal structure also determines the specific capacity via the amount of ions that can be extracted/inserted into the structure without it being destroyed.[3] Deviations from the ideal crystal

structure can affect the battery function in a good or a bad way. For example, crystal defects in hydrothermally synthesized $LiFePO_4$ close ion diffusion pathways resulting in a reduction of the specific capacity.[6] It is obvious, therefore, that the crystal structure plays an essential role in determining the energy density of the electrode material. The size and morphology of the electrode material particles and crystallites has similarly been shown to influence the energy density and other properties of the electrode material significantly. It can alter the electrochemical performance of a material in a positive or a negative way.[7] Having smaller crystallite sizes means shorter diffusion pathways within the bulk of the crystallites.[8] The short diffusion lengths can sometimes, as in the case of nanosized rutile-TiO_2, define whether a material is electrochemically active or not.[9] Nanosizing can also affect the rate capability, i.e., how fast the cell can be charged and discharged. The reason being that shorter diffusion lengths lead to shorter ion diffusion times. Furthermore, the higher specific surface area of nanosized materials allows for higher probability of ions entering the crystal structure.[8] The morphology of the electrode material particles and crystallites can also play a role in the rate capability, especially in the case of materials exhibiting either one dimensional (1D) or two dimensional (2D) Li-ion diffusion where specific morphologies allow for relatively large areas for insertion of Li-ions and short diffusion pathways within the crystallites. Thus it is very important to be able to control crystal structure, phase purity, crystallite sizes and morphology when synthesizing electrode materials. This would, in principle, allow for tuning of the battery properties to suit different applications.

1.2 Synthesis

As explained in detail in the previous chapter the crystal structure, crystallite size and morphology affect battery performance. Controlling those properties via the synthesis is therefore important in order to optimize battery packs for specific applications.

1.2.1 Solvothermal synthesis

Solvothermal synthesis is defined as a chemical reaction in a closed reaction vessel, e.g. autoclave, at temperatures above the boiling point of the solvent. When using water as solvent the method is termed hydrothermal synthesis.[10] The pressure is elevated autogenously in an autoclave or alternatively externally by pumps in a flow system. This keeps the solvent from evaporating at high temperatures. The elevated temperatures lead to very drastic changes in the physical properties of the solvent. For example, the dielectric constant of water is only half its value at 200°C compared to room temperature (RT). In solvothermal synthesis supercritical conditions (374°C and 221 bar for water) can be achieved giving relatively abrupt change in physical properties compared to sub-critical conditions.[11] The solvothermal synthesis method has been proven as a successful tool to synthesize a wide variety of crystalline phases with tunable features e.g. crystallite size and morphology, by tuning different synthesis parameters, e.g., precursor composition and concentration, pH, reaction time, temperature and pressure.[12]

1.3 Characterization

As described previously, certain structural features of the electrode materials can be connected to performance properties of battery packs. It is consequently very important to be able to characterize the crystalline structure of the electrodes well. My research, until now, has mainly been focused on characterizing the electrode material structure *in situ*, i.e. during synthesis, using powder X-ray diffraction (PXRD) and total scattering (TS) using X-rays. The *in situ* characterization of

solvothermal reactions, described in detail below, gives a unique opportunity to control and understand the synthesis of crystalline materials. PXRD characterizes the average crystalline structure giving valuable information about the crystalline reaction product. TS, in combination with pair distribution function (PDF) analysis, is a very powerful characterization tool because it enables the possibility of probing local and global correlations. It therefore allows for detection of both non-crystalline and crystalline materials in the reaction solution, e.g. amorphous material, metal complexes and crystals. This knowledge can lead to a deeper and more profound understanding of the reaction mechanism compared to an *in situ* study based solely on PXRD. In the following sections a brief introduction to PXRD, TS and the analysis of the respective types of data will be presented.

1.3.1 Powder X-ray diffraction

PXRD is a powerful tool to probe the average structure of crystalline materials. All electromagnetic radiation (light) is scattered by electrons in atoms. When X-rays scatter from crystals, they interfere to produce diffraction patterns with sharp peaks uniquely related to a given crystal structure. Diffraction is possible because the wavelength of X-rays is in the same order of magnitude as chemical bond lengths, and atomic arrangements in crystals are periodic. In fact, a material is defined to be a crystal if it exhibits sharp diffraction peaks.[13] For a powder sample, i.e. where a large number of crystallites are orientated randomly, the diffracted X-ray beams form concentric cones (called Debye-Scherrer cones). The diffraction pattern is recorded as intensity as function of 2θ-angle, i.e. the angle between the direct beam and the diffracted beam.[14]

The positions of the diffraction peaks can be described by Bragg's law:

$$2d\sin(\theta) = n\lambda$$

Where d is distance between parallel crystallographic planes (denoted by hkl indices), θ is the angle between the direct beam and the crystallographic plane ($\theta = {}^{1}/_{2}\,2\theta$), n is the order of diffraction (usually taken to be equal to one because the first order diffraction is the most prominent one) and λ is the wavelength of the X-ray beam. The 2θ positions of the set of Bragg peaks in the diffractogram then give information about the unit cell dimensions and selection rules, i.e. set of missing peaks, give information about the crystal symmetry.[15]

The intensity of a given hkl Bragg peak is proportional to the square of the structure factor F_{hkl} given by:

$$F_{hkl} = \sum_{j=1}^{N} o_j f_j(\theta_{hkl}) e^{-B_j \frac{\sin^2\theta_{hkl}}{\lambda^2}} e^{2\pi i(hx_j + ky_j + lz_j)}$$

The sum runs over all atoms in the unit cell, o_j is the site occupancy, $f_j(\theta_{hkl})$ is the atomic form factor (function of scattering angle), B_j is the atomic temperature factor and (x_j,y_j,z_j) are the fractional coordinate of the j^{th} atom in the unit cell. The intensity of the set of hkl Bragg reflections therefore contains information about the identity, position and thermal motion of the atoms in the unit cell. This, together with the unit cell dimension and symmetry, gives information about the crystal structure.[15]

If the crystals in the powdered sample are ideal, i.e. have long range periodicity (large crystals), and are defect and strain free, the width of the Bragg peaks is determined by the instrumental resolution. If the crystals on the other hand are small and/or are strained the Bragg peaks are broadened compared to the instrumental resolution. As a result, information on the size of coherently scattering crystal domains (crystallites) and microstrain can be extracted by analyzing the peak profile of broadened Bragg peaks. Size and microstrain broadening differ independently as a function of diffraction angle and can consequently be discriminated if data is measured up to high angles. The volume averaged crystallite size can be calculated using the Scherrer equation:

$$\langle D_{hkl} \rangle = \frac{K_{hkl}\lambda}{\beta_{hkl}\cos(\theta_{hkl})}$$

Where β_{hkl} is the integral breadth of the hkl Bragg peak and K is a constant close to one depending on the hkl index of the given Bragg peak and shape of the crystallite.[16]

1.3.1.1 Rietveld refinement

Rietveld refinement is a powerful tool to extract structural information from a PXRD pattern. The goal in this method is to minimize the difference between a collected PXRD pattern and a pattern calculated based on a structural model. This means minimizing the residual (S) in a least squares refinement.

$$S = \sum_i w_i (y_i - y_{ci})^2$$

Where $w_i = {}^1/_{\sigma_i^2}$ is a weighing factor giving less weight to data points with high uncertainty, y_i is the observed intensity in data point i and y_{ci} is the calculated intensity at data point i. The intensity of point i is calculated based on a structural model applying:

$$y_{ci} = \sum_p s_p \sum_{hkl} L_{hkl} |F_{hkl}|^2 \varphi(2\theta_i - 2\theta_{hkl}) P_{hkl} A + y_{bi}$$

Here s_p is the scale factor of phase p. L_{hkl} is the Lorentz polarization and multiplicity factors. φ is a profile function and P_{hkl} is a function describing preferred orientation of the crystallites in the samples. A is an absorption factor and y_{bi} is the background intensity at point i. In the Rietveld refinement all of these parameters can be refined to get information about the crystalline part of a sample. For example, one can calculate the weight fractions of crystalline phases in the sample from the relative values of scale factors. Of course, as in any least squares minimization, a good initial guess, i.e. a structural model close to the true structure, is essential for finding the true global minimum of the residual. Furthermore, because the function for the calculated intensity is multidimensional, care has to be taken to only refine few parameters at a time until the residual is close to a minima.[17]

In my work I have used the program package FullProf Suite to perform Rietveld refinements.[18] Refinements are normally carried out by loading a structural model via a crystallographic information file (CIF) (more than one if multiple phases are present) and refining structural and instrumental parameters such as unit cell dimensions, background and zero point. In this work the peak broadening is assumed to be purely from crystallite size, which is often the dominating effect

in crystallites grown from solution. I do this to simplify the model used in Rietveld refinements, ensuring that only the most relevant parameters are used to fit relatively poor data. Crystallite sizes are calculated from refined peak profiles where the instrumental profile is taken into account by loading an instrumental resolution file (IRF). The IRF is obtained by refining a PXRD pattern of a NIST standard LaB_6 sample where the peak profile is assumed to be purely due to instrumental effects. The crystallite sizes can be assumed isotropic or anisotropic using different models. In my work anisotropic crystallite sizes are refined using either a model assuming cylindrical shape with principle axis along a chosen crystallographic direction (platelet/needle model)[19] or a more general model using spherical harmonic functions.[18, 20]

1.3.2 Total scattering and the pair distribution function

In Rietveld refinements of PXRD data only the intensities and profile information from the Bragg peaks are taken into consideration. This means the average crystalline structured is probed and no information about short range order, i.e. the local environment of the atoms, is obtained. The information about short range order is contained in diffuse scattering between and under the Bragg peaks and is normally just modelled as background in Rietveld refinements.[21] By Fourier transforming the total scattering intensity, I(Q), in the form of the reduced structure function, F(Q), a function called the reduced pair distribution function can be obtained:

$$G(r) = \frac{2}{\pi}\int_{Q_{min}}^{Q_{max}} F(Q)\sin(Qr)\,dQ$$

$$F(Q) = Q\left(\frac{I(Q)}{\langle b\rangle^2} - 1\right)$$

Q is the scattering vector ($Q = {}^{4\pi\sin\theta}/_{\lambda}$), $\langle b\rangle$ is the average scattering power and r is a distance in real space. Note that in order to perform a proper Fourier transform total scattering data would have to be measured to from zero infinite Q. Fortunately this is not necessary in practice, because the total scattering intensity falls to zero at high Q owing to the thermal motion of the atoms. Often it is sufficient to collect data up to 20 $Å^{-1}$ although higher Q_{max} results in higher resolution in real space.

The reduced pair distribution function is also given by:

$$G(r) = \frac{R(r)}{r} - 4\pi r\rho_0$$

Where ρ_0 is the average number density in the sample (electron density in the case of X-ray scattering) and R(r) is the radial distribution function (RDF) given by:

$$R(r) = \sum_\nu \sum_\mu \frac{b_\nu b_\mu}{\langle b\rangle^2}\delta(r - r_{\nu\mu})$$

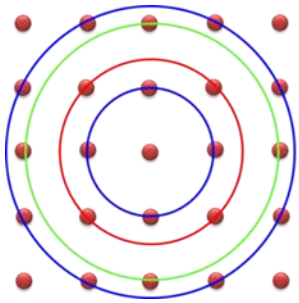

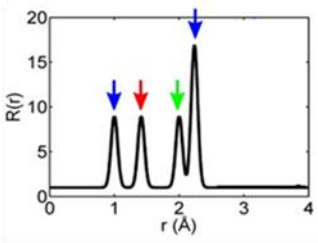

The physical meaning of the RDF is visualized in Figure 1. The RDF has a peak every time a sphere of radius r around every atom in the material meets other atoms in the material. The

Figure 1: Physical meaning of the radial distribution function, Graphics by Dr. Dipankar Saha.

integrated intensity of the peak ($\int R(r)dr$) is proportional to the number of atoms in an annulus of thickness dr and the scattering power of the atoms.[22]

By collecting total scattering data up to high Q and calculating the reduced pair distribution functions it is possible to obtain information about all interatomic distances in the measured sample. Thus, information can be obtained about the short range order, e.g., nearest neighbor distances in amorphous materials and bond distances in dissolved complexes, as well as the long range order observed in crystals. The medium range order found in nanocrystalline materials, where the coherence length is in the order of a few nanometers, is also apparent from this method.

1.3.2.1 Real space refinements

Information about bond lengths and coordination numbers can be extracted directly from the PDF. Nevertheless it is possible to extract much more information from the PDF by comparing the data to a structural model and performing real space refinement of structural parameters. The results might quantifiably indicate what structures are present in the sample and what the coherence length of those structures are.[23]

In this work, real space refinements against PDF-data were carried out using the program PDFgui where structures are loaded via CIF. PDFgui uses a least squares refinements routine to fit a model to the data giving the possibility to refine scale factors, unit cell, coherence length along with many other structural and instrumental parameters.[24]

1.3.3 *In situ* characterization of solvothermal synthesis

In order to tune the properties of solvothermal synthesis products, a comprehensive understanding of the effect of different synthesis variables are needed. This can be a very extensive and often tedious task, especially by *ex situ* measurements, where every possible variable is systematically changed and the products characterized after the reaction has been stopped. *In situ* measurements open the possibility to measure different properties in real time while the reaction happens. This greatly simplifies the parametric study since effects of variables such as reaction time and temperature can be seen immediately.[25] Another advantage of *in situ* measurements is that they provide time resolved data of the reaction, meaning reaction kinetics and relative stabilities of different reaction products can be observed.[26, 27] *In situ* measurements are not always straight forward, especially in the case of solvothermal reactions where the reaction normally takes place within steel autoclaves or closed flow systems at high temperatures and pressures. Our research group has developed and successfully implemented a reactor allowing for *in situ* characterization of solvothermal reactions using PXRD and TS.[28-32]

A schematic view of the setup is seen in Figure 2. The solvothermal reaction happens within a thin capillary made of single crystalline sapphire for PXRD measurements and fused silica for PDF measurements. The reaction solution is pressurized by a HPLC pump using the appropriate solvent. The synthesis is started by external heating from a hot air blower. The high air flow and small volume of the capillary

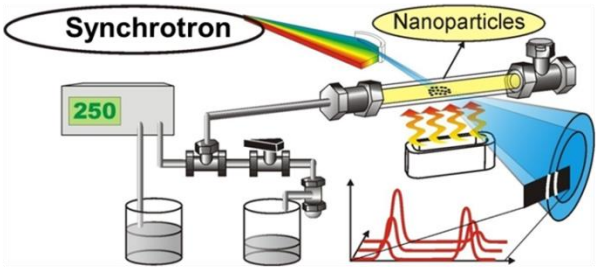

Figure 2: Schematic view of the *in situ* solvothermal reactor. Graphics by Dr. Mogens Christensen.

ensures that steady state temperature is reached within a few seconds. The temperature is controlled by a PID controller which can be set to maintain an isothermal reaction temperature or ramped up and down. Note that due to heat losses from the hot air nozzle to the capillary the actual reaction temperature is approximately 2-10% lower than the set point temperature (SPT). The actual reaction temperature is determined by temperature calibration. Time resolved PXRD or total scattering patterns are collected at various synchrotron sources and by the use of an area detector. The very high brilliance of synchrotron radiation, compared to laboratory sources, is necessary to be able to collect the data with high enough time resolution. Also for calculating the PDFs it is necessary to collect data up to high Q meaning a high energy (low wavelength) beam is needed. The individual data files containing 2D scattering intensities collected in a given time frame are integrated in order to obtain scattering intensity as a function of 2θ or Q. The PXRD data frames are then ready for sequential Rietveld refinements. In contrast, the total scattering intensity must be corrected and Fourier transformed first in order to obtain time resolved PDF, which then is refined sequentially in real space.[32]

2 Materials and results

During the first 2 years of my PhD research I have mostly focused on *in situ* hydrothermal synthesis and characterization of two different cathode materials, spinel type $LiMn_2O_4$ and various distinct structural phases of MnO_2. The following sections will discuss the work conducted thus far on these materials applying the techniques described in the previous section.

2.1 Spinel type $LiMn_2O_4$

Spinel type $LiMn_2O_4$ (LMO) has received a great deal of attention as a positive electrode material for use in Li-ion batteries, and is considered a possible alternative to the widely used $LiCoO_2$. LMO is cheaper, more environmentally benign,[33] and it has already been commercialized in lithium ion battery packs. LMO crystallizes in the cubic space group $Fd\bar{3}m$ with unit cell parameter $a = 8.248$ Å in the bulk phase. It has the normal spinel structure with the Li-ions residing in 1/8 of the tetrahedral holes and the Mn-ions in ½ of the octahedral holes in a cubic close packed array of oxygen anions.[34]

2.1.1 Synthesis

LMO can be synthesized in a variety of ways,[35] including hydrothermally. The hydrothermal method has been shown to produce LMO nanocrystallites[36, 37] with varying morphology, from spherical to needle shaped.[38] It has been demonstrated that nanocrystalline LMO has higher specific capacity and better rate capability compared to large LMO crystallites. The improved capacity and rate capability is attributed to less repulsion between Li-ions at the surface and shorter diffusion lengths within the bulk.[39, 40] Nanosizing LMO increases the specific surface area, and this in turn can pose other problems including dissolution of manganese by the electrolyte.[41]

In this work, LMO is synthesized hydrothermally by reduction of $KMnO_4$ in an aqueous solution containing Li-ions from LiOH, where ethanol is included as a reducing agent. The balanced chemical reaction equation is:

$$(1)\ 4LiOH_{(aq)} + 8KMnO_{4(aq)} + 7CH_3CH_2OH_{(l)} \xrightarrow{\Delta} 4LiMn_2O_{4(s)} + 8KOH_{(aq)} + 7CH_3COOH_{(l)} + 5H_2O_{(l)}$$

This synthesis route was first proposed by Liddle *et al.*[36] using a variety of organic reducing agents, such as alcohols or ketones. It has been reported that this synthesis route is capable of producing phase pure LMO nanocrystallites but with lower than optimal specific capacity, and appearance of impurity phases using less than optimal reaction conditions.[36, 42] An *in situ* characterization of the synthesis is therefore interesting to attempt to understand why these shortcomings arise and determine how to optimize the synthesis and thus the properties of the products.

2.1.2 *In situ* PXRD characterization

The *in situ* PXRD study of hydrothermal formation of LMO nanocrystallites was performed on beamline I711MAX II at MAX-lab in Lund, Sweden (March 2013). The study experimented with the following synthesis parameters (presented in Table 1); isothermal reaction temperature, LiOH concentration and the use of different alcohols as reducing agents. In all the experiments the pressure was kept constant at 250 bars.

Table 1: Overview if synthesis parameters for *in situ* study of LMO synthesis (SPT=Set Point Temperature)

Reaction solution	Molar ratio (Li:Mn:Redox)	Reducing agent	SPT 220°C	SPT 260°C	SPT 300°C	SPT 350°C	SPT 400°C
1	2:1.0:3.4	Ethanol	√	√	√		
2	0.8:1.0:3.4	Ethanol	√	√	√		
3	0.4:1.0:3.4	Ethanol	√	√	√		
4	0:1.0:3.4	Ethanol	√	√	√		
5	0.5:1.0:3.4	Ethanol	√	√	√	√	√
6	0.5:1.0:3.4	Methanol	√	√	√		
7	0.5:1.0:3.4	Propanol	√	√	√		
8	0.5:1.0:3.4	Propan-2-ol	√	√	√		
9	0.5:1:0.875	Ethanol	√	√	√		

2.1.2.1 Temperature study

The most promising results for LMO production were obtained during the temperature study (SPT=220, 260, 300, 250 and 400°C), i.e. reaction solution 5. From the given molar ratio, the Li:Mn ratio is stoichiometric, however, the solution contains excess reducing agent, ethanol. These results have been published in a scientific paper in the journal Dalton Transactions.[43] A brief description will be given here to highlight the important findings from this article, but the reader is directed to the full paper for a more comprehensive discussion.

Analysis of the time resolved PXRD for each of the five temperatures reveals the reaction mechanism of this hydrothermal synthesis system. It can be summarized in the following reaction steps (a-c):

$$(a)\ 2LiOH_{(aq)} + 4KMnO_{4(aq)} + 3CH_3CH_2OH_{(l)} \xrightarrow{RT} 4\,\delta - MnO_2 \cdot (LiOH, KOH, xH_2O)_{(s)} + 3CH_3COOH_{(l)} + H_2O_{(l)}$$

$$(b)\ 8\delta - MnO_2 \cdot (LiOH, KOH, xH_2O)_{(s)} + CH_3CH_2OH_{(l)} \xrightarrow{\Delta} 4LiMn_2O_{4(s)} + 8KOH_{(aq)} + CH_3COOH_{(l)} + 3H_2O_{(l)}$$

$$(c)\ 12LiMn_2O_{4(s)} + 5CH_3CH_2OH_{(l)} + H_2O_{(l)} \xrightarrow{\Delta} 8Mn_3O_{4(s)} + 12LiOH_{(aq)} + 5CH_3COOH_{(l)}$$

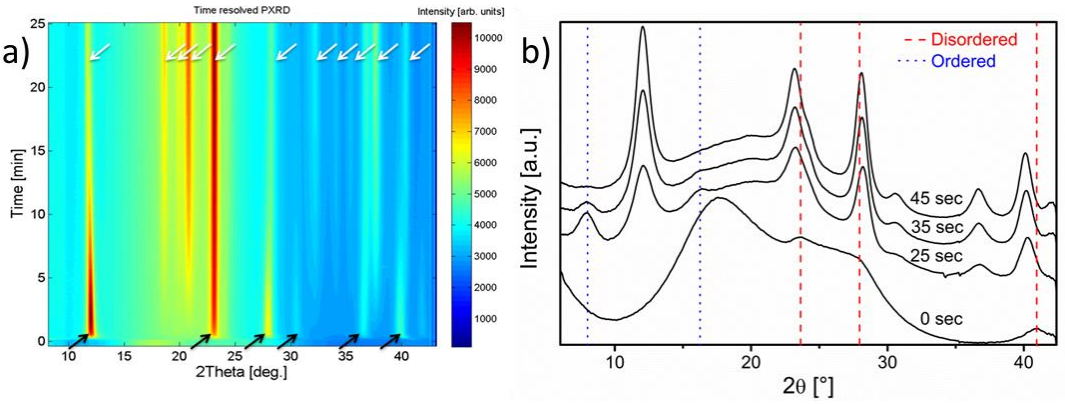

Figure 3: PXRD data for reaction solution 5; a) Time resolved PXRD data collected at SPT=260°C, black arrows indicate LMO reflections and white Mn_3O_4 reflections, and b) Selected frames at 260°C showing disordered δ-MnO_2 before reaction initiation and appearance and disappearance of ordered δ-MnO_2.

At RT, $KMnO_4$ is reduced by ethanol yielding disordered δ-MnO_2 according to reaction (a). This is seen by broad Bragg reflections in the PXRD pattern before reaction initiation (see 0 sec in Figure 3b). δ-MnO_2 has a layered structure with MnO_2 sheets and different interlayer species (probably K^+, Li^+ and H_2O in this case). The degree of ordering in the structure depends on how well aligned the MnO_2 sheets are and on the degree of ordering amongst the interlayer species.[44] The structure is described in greater detail in the chapter 2.2.1.4. Shortly after the reaction is initiated, the degree of ordering in δ-MnO_2 increases. This is seen by appearance of Bragg reflections characteristic for interlayer ordering of δ-MnO_2 after short reaction time (see Figure 3b). The ordering is observed at all temperatures studied, except at 400°C. The reaction continues during heating and the δ-MnO_2 is reduced further to the desired LMO nanocrystallites according to reaction (b). This is seen by disappearance of the δ-MnO_2 Bragg reflections and appearance of broad Bragg reflections that can be indexed to spinel type LMO (see Figure 3b). For all temperatures the LMO Bragg reflections disappear with extended reaction time and reflection belonging to the Mn_3O_4 phase appear (see Figure 3a). This behavior indicates that LMO is reduced to Mn_3O_4 by residual ethanol in the reaction solution according to reaction (c). Mn_3O_4 has a very similar structure to LMO, being tetragonally distorted spinel type, but now the tetrahedral sites are filled with Mn^{2+} ions and the octahedral sites with Mn^{3+} ions.[45] Figure 4a shows the refined weight fraction of LMO crystallites in the reaction solution at different temperatures. The figure shows how much of the LMO crystallites have transformed into Mn_3O_4 as a function of reaction temperature. It is evident that increasing the reaction temperature increases the reaction rate. This is expected since higher temperature generally leads to higher reaction rates in chemical reactions.[46] The *in situ* data obtained here could possibly be used for determining rate constants, activation energy and rate determining steps. This is not done since to my knowledge there is no well-established model describing growth of crystals in a solvothermal synthesis. I have also seen in some of my studies that systems with manganese containing particles do not exhibit the same rate even at the same experimental configuration. Therefore I would only attempt to extract kinetic information if the reproducibility of the system is thoroughly tested, which is not the case here.

Based on these experiments it can be stated that LMO nanocrystallites are unstable in this reaction system, transforming to Mn_3O_4 which is electrochemically inactive in Li-ion cathodes. This means that careful tuning of the reaction conditions is necessary in order to obtain phase pure LMO and

consequently the cathode material with the highest possible specific capacity. Figure 4a offers the information needed to obtain phase pure LMO by controlling reaction temperature and time. It shows that the reaction solutions at set point temperature equal to 220 and 260°C contain phase pure LMO in the respective time intervals 150-210 sec and 45-140 sec. At 300 and 350°C some Mn_3O_4 has already formed at the time where all δ-MnO_2 has disappeared, thus giving a mixture of phases throughout the reaction process. Note that in order to implement those results directly to a realistic synthesis setup, i.e. setup capable of producing considerable amount of product, the heating rate would have to be matched. Other factors of the in situ experimental setup, such as small fluctuations in the temperature and the fact the reaction is happening within a capillary, might also skew these results when applied on a large scale. Inspecting the proposed reaction mechanism gives rise to the hypothesis that phase pure LMO might be obtained by using stoichiometric amounts of reducing agent, i.e. all the reducing agent would be used upon LMO formation and no further reduction to Mn_3O_4 can occur. This hypothesis was tested and found to be wrong. Three more *in situ* experiments, using reaction solution 9 (see Table 1), containing stoichiometric amount of ethanol were performed as tests. The final composition in these experiments was a mixture of LMO and Mn_3O_4 indicating that as soon as some LMO is produced it immediately starts converting to Mn_3O_4, i.e. before the reducing agent is used to transform all the MnO_2 to LMO. Based on these observations, the phase purity of LMO cannot be controlled by varying the amount of ethanol in the synthesis.

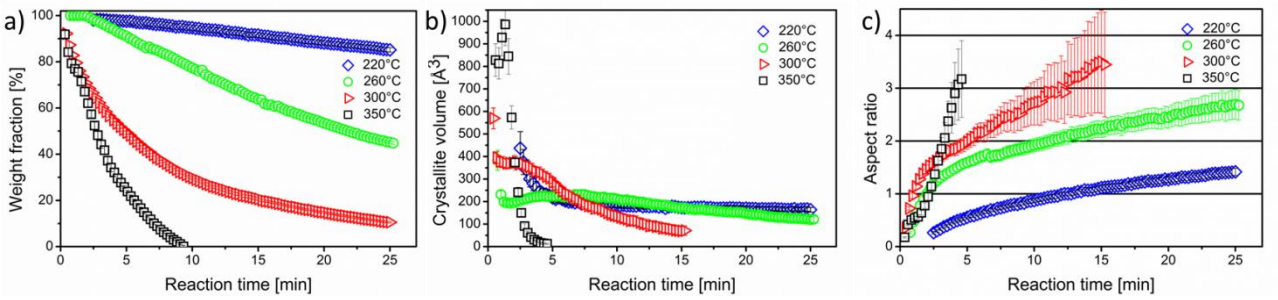

Figure 4: Results from temperature study (reaction solution 5) as a function of reaction time for different reaction temperatures a) Weight fraction of LMO (rest is Mn_3O_4) b) Crystallite volume [$Å^3$] c) Aspect ratio of cylindrically shaped crystallites.

Using sequential Rietveld refinements, information about the evolution of crystallite size and morphology as a function of reaction time is extracted. These refinements suggest that the crystallites are formed as nanocrystallites with characteristic lengths in the range of 2-25 nm. The best fit to the PXRD patterns was obtained by using a platelet/needle model[19] for the crystallite shape with the principle axis along the crystallographic [111] direction. In Figure 4b the crystallite volume at different reaction temperatures is plotted as a function of reaction time. It shows higher reaction temperature leads to larger initial crystallites. During the course of the reaction, the crystallite volume decreases, this agrees well with the fact that LMO is transforming into Mn_3O_4. The aspect ratio (needle length/diameter) at different reaction temperatures is plotted as a function of reaction time in Figure 4c. At all temperatures the crystallites are initially thin platelets (aspect ratio << 1). The fact that the aspect ratio has the same initial value at all temperatures indicates that the initial crystallites are formed from the δ-MnO_2 crystallites which are already present at room temperature. As the reaction continues further the aspect ratio increases reaching approximately spherical crystallites (aspect ratio ≈ 1) and continues to grow into rod shaped crystallites (aspect

ratio > 1). Note that the estimated standard deviation (esd) of the refined parameters and the quantities calculated from them are based on the quality of the fit obtained in the Rietveld refinements. This means that random and systematic errors due to the instrument and or experimental setup are not taken into account. Random error from the experimental setup might be estimated by running multiple experiments at the same reaction conditions but is not done here because of limited beamtime.

2.1.2.2 Effect of LiOH concentration

The effect of LiOH concentration in the reaction solution was studied by making four different reaction solutions (1-4 in Table 1). The data obtained on the effect of LiOH concentration has been analyzed in less detail compared to the temperatures study discussed above. Only preliminary Rietveld refinements are performed and most of the conclusions drawn are based on qualitative analysis of the time resolved PXRD patterns.

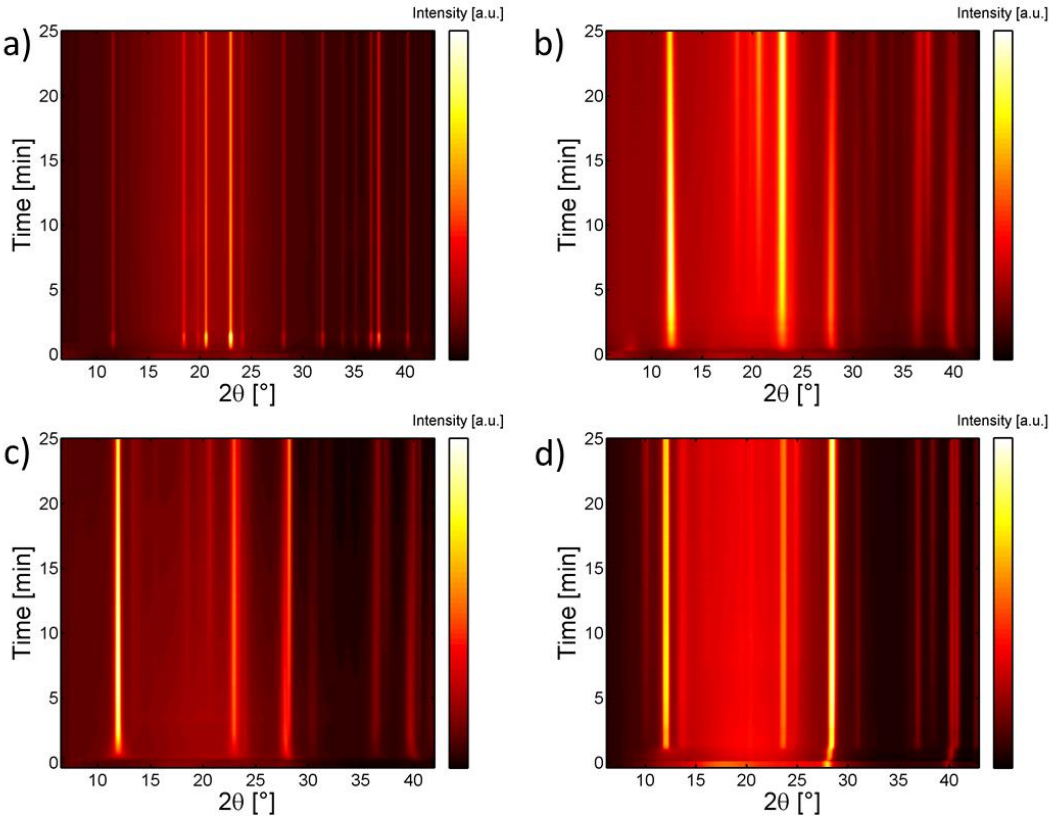

Figure 5: Time resolved PXRD data at 260°C of reaction solutions varying in LiOH concentration a) Li;Mn:EtOH=0:1.0:3.4 b) Li;Mn:EtOH=0.4:1.0:3.4 c) Li;Mn:EtOH=0,8:1.0:3.4 d) Li;Mn:EtOH=2:1.0:3.4.

Each reaction solution was reacted at set point temperatures 220, 260 and 300°C. The only effect of temperature observed was a higher reaction rate at higher temperature and this will therefore not be discussed further. Figure 5a shows the time resolved PXRD data for the reaction solution containing no LiOH. It is observed that disordered δ-MnO_2 transforms directly into large Mn_3O_4 crystallites with no appearance of an ordered δ-MnO_2 phase. No further change is observed after Mn_3O_4 has formed. The Mn_3O_4 crystallites are said to be large because the peak broadening is solely determined by instrumental broadening, i.e. the crystallites are too big to measure with the instrument used. The experiment with the LiOH concentration equal to zero (reaction solution 4)

was performed as a baseline experiment for studying the effect of Li-ions, and alkaline environment on the synthesis. Unsurprisingly no LMO is formed, simply because there are no Li-ions in the solution. It is however observed that the end product, i.e. Mn_3O_4, is unchanged. Thus, the presence of Li-ions in the solution allow for Mn-ions to crystallize in an intermediate oxidation state (averaging to +3.5) in the LMO phase. Furthermore it is evident that micrometer sized Mn_3O_4 crystallites can be produced hydrothermally using this reaction solution at relatively short reaction times and low temperatures.

Figure 5b shows time resolved PXRD patterns of the reaction solution containing Li:Mn:EtOH=0.4:1.0:3.4 molar ratio (reactions solution 3). Qualitatively, this reaction solution shows the same result as the reaction solution used in the temperature study discussed above.

Figure 5c presents the time resolved PXRD patterns of the reaction solution containing Li;Mn:EtOH=0.8:1.0:3.4 molar ratio (reaction solution 2). Similarly to what was observed for the reaction solutions with lower LiOH concentration, disordered δ-MnO_2 is observed at RT with increased ordering upon heating followed by a transformation to LMO. Shortly thereafter new Bragg reflections appear indicating the appearance of layered $Li_xMn_yO_2$ crystalline phase in the reaction solution. The PXRD patterns for LMO and $Li_xMn_yO_2$ are almost identical but the indicator for $Li_xMn_yO_2$ emergence is a splitting of the Bragg reflection at $2\theta \approx 40°$ and a broad peak at $2\theta \approx 13°$ suggesting superstructure ordering in the layered structure. The LMO and lithium rich $Li_xMn_yO_2$ phase co-exist, either because they both grow from the δ-MnO_2 or LMO is transformed into $Li_xMn_yO_2$. It is further observed that as the reaction continues Bragg reflections from Mn_3O_4 appear and the reflections from both LMO and $Li_xMn_yO_2$ disappear.

Time resolved PXRD patterns of the reaction solution containing Li:Mn:EtOH=2:1.0:3.4 (reaction solution 1) are presented in Figure 5d. The first thing to notice is small amount of Mn_3O_4 seemingly present at a constant amount throughout the synthesis. This most likely stems from the use of a dirty sapphire tube containing Mn_3O_4 from previous data collection runs. Alternatively this may indicate that some Mn_3O_4 is produced at RT and does not participate in the reaction. It is hard to determine which one of those possibilities is true because it was not immediately evident, and no further beamtime was available to repeat these reactions. If the Mn_3O_4 detected in the PXRD pattern is due to the synthesis, then the synthesis product will always contain some amount of Mn_3O_4 impurity irrespective of the reaction time. Upon inspection of the PXRD patterns obtained at RT it is seen that disordered δ-MnO_2 is present in relatively large amounts. Ordering of the δ-MnO_2 is not observed upon heating and there is no clear appearance of LMO. Instead a direct transformation to the layered $Li_xMn_yO_2$ is observed. An unidentified phase appears briefly after $Li_xMn_yO_2$ has formed and grows slowly throughout the synthesis. As stated before the Bragg reflections due to Mn_3O_4 do not change throughout the synthesis. It therefore seems that the $Li_xMn_yO_2$ phase and the unidentified phase do not transform into Mn_3O_4, at least not in the measured timespan of the reaction.

The results of the LiOH concentration study shows us that the presence of LiOH in low concentration in the reaction solution allows for the production of LMO. At higher LiOH concentrations lithium rich $Li_xMn_yO_2$ phase co-exists with LMO resulting in an impure LMO sample. It is further seen that if LMO is produced it is always unstable toward further reduction into Mn_3O_4. Very high LiOH concentration seems to inhibit the growth of Mn_3O_4 however that does not matter since no LMO is produced, instead a mixture of $Li_xMn_yO_2$ and an unidentified phase is observed.

2.1.2.3 Effect of different reducing agents

The effect of varying the reducing agent used in the synthesis was examined by studying four different reaction solutions with the molar ratio Li:Mn:reduct=0.5:1.0:3.4 and varying the reducing agent between methanol, ethanol, propanol and propan-2-ol, see reaction solutions 5-8 in Table 1. The results presented here are based on rough Rietveld refinements and qualitative analysis of the time resolved PXRD patterns.

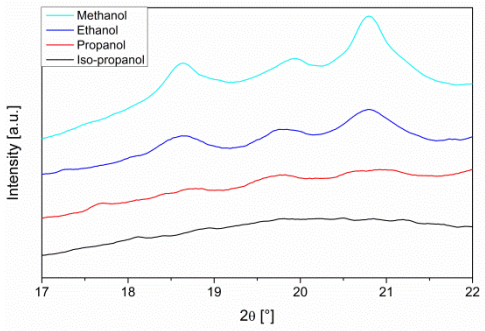

Figure 6: The 3 characteristic peaks of Mn_3O_4 after 8 minutes of reaction at 260°C using different reduction agents.

Each reaction solution was conducted at set point temperatures ranging from 220 to 300°C. The only effect of using different reducing agent was found to be changes in the reaction rate of the δ-MnO_2 to LMO and LMO to Mn_3O_4 transformation. This is demonstrated by the results given in Figure 6 showing the PXRD patterns for all the different reducing agents in the range 2θ=17-22°, where the three characteristic peaks from Mn_3O_4 are present. All the PXRD patterns are collected after 8 minutes of reaction at SPT=260°C. The reaction solution containing methanol led to the largest amount of Mn_3O_4 produced, ethanol less, propanol only very small amounts. In the case of propan-2-ol, no Mn_3O_4 is visually observed after 8 minutes of reaction. This means the reaction rate increases with different reducing agents in the following order: propan-2-ol<propanol<ethanol<methanol. This difference may be attributed to the degree to which the different alcohols may be oxidized. It has been shown[47] that the oxidative activity of the alcohols studied here in alkaline solution is methanol<propanol<ethanol<propan-2-ol giving almost the opposite trend observed from the *in-situ* results produced here. These results are quite contradictory but could be explained by the difference in temperature used in this study (220-300°C) whereas the oxidative activity described in literature was determined at RT.

2.2 MnO_2

MnO_2 is an important functional material with versatile applications ranging from catalysis to electrochemistry.[48-50] Different crystalline MnO_2 phases have been used as positive electrode materials in LIBs and SIBs.[51, 52] MnO_2 finds further applications as an electrode material in super-capacitors.[53] The material is a common metal oxide and exists in a variety of crystalline forms, e.g. tunneled, layered and spinel type structures. Many of the different MnO_2 phases can be synthesized solvothermally by varying the precursor and modifying the reaction conditions, raising an interesting question: why does a particular crystalline phase form under particular solvothermal conditions? This question is especially compelling when the possibility of crystalline phases is as broad as in the case of MnO_2. *In situ* total scattering characterization of solvothermal syntheses is one way in which some answers to this question may be gleaned. Using this technique it is possible to observe metal complexes in the reaction solution together with amorphous and crystalline material throughout the synthesis. Insight into the fundamental formation mechanisms involved under different reaction conditions can thus hopefully be achieved. In addition, practical information about how to optimize the synthesis of the different phases and how to tune (micro)-structural features such as crystallite size, morphology and others may be obtained. In this *in situ* study, four different hydrothermal syntheses towards production of α-, β-, γ- and δ-MnO_2 were

examined in order to obtain answers about how and why they form under specific conditions. It must be noted here that preliminary work on the precursors and reaction conditions that are needed to synthesize pristine samples were performed by a dear colleague of mine, Dr. Yanbin Shen. Her work was invaluable in order to get the most out of the limited time available at the synchrotrons.

2.2.1 Synthesis

2.2.1.1 β-MnO_2

β-MnO_2 crystallizes in the well-known rutile structure type. Its space group is the tetragonal $P\,4_1/m\,n\,m$ and has unit cell parameters $a = 4.3983$Å, $c = 2.873$Å.[54] The structure can be described as infinite chains of edge sharing MnO_6 octahedra that interlink by corner sharing, see Figure 7a. There are tunnels with dimensions of 1x1 octahedra along the crystallographic [001] direction.[44]

The hydrothermal synthesis of β-MnO_2 involves heating an aqueous solution of $Mn(NO_3)_2$ under pressure. Possible reaction mechanism is presented in (2)[55] although the likelihood of it may be questioned based on the limited amount of dissolved O_2 in the reaction solution. Other reaction mechanisms, where O_2 doesn't participate, may be more appropriate.

$$(2) \quad 2Mn(NO_3)_{2(aq)} + O_{2(aq)} + 2H_2O_{(l)} \xrightarrow{\Delta} 2MnO_{2(s)} + 4HNO_{3(aq)}$$

The precursor solution used here was prepared by dissolving $Mn(NO_3)_2$ in water to a Mn^{2+} concentration of 4.0 M.

2.2.1.2 γ-MnO_2

γ-MnO_2 crystallizes in the monoclinic space group $C\,2/m$ and has unit cell parameters $a = 13.7$ Å, $b = 2.9$ Å, $c = 4.5$ Å and $\beta = 90.5°$.[56] A representation of the crystal structure using MnO_6 octahedra can be seen in Figure 7b. Like β-MnO_2 it consists of infinite edge sharing chains but by additional edge sharing between two chains, creates 2x1 and 1x1 tunnels.[44]

The hydrothermal synthesis of γ-MnO_2 involves oxidation of $MnSO_4$ to MnO_2 by $(NH_4)_2S_2O_8$ and is given in reaction scheme (3).[55]

$$(3) \quad MnSO_{4(aq)} + (NH_4)_2S_2O_{8(aq)} + 2H_2O_{(l)} \xrightarrow{\Delta} MnO_{2(s)} + (NH_4)_2SO_{4(aq)} + 2H_2SO_{4(aq)}$$

The precursor solution used here was prepared by dissolving $MnSO_4$ in water to a Mn^{2+} concentration of 0.8 M and then adding $(NH_4)_2S_2O_8$ powder to obtain a NH_4^+ concentration of 1.6 M.

2.2.1.3 α-MnO_2

The α-MnO_2 structure can be described as infinite chains of edge sharing MnO_6 octahedra that connect to neighboring chains either by edge sharing or corner sharing (see Figure 7c). The tunnels formed, stretching out along the crystallographic [001] direction, have dimensions of either 2x2 or 1x1 octahedra. The 2x2 tunnels are wide enough to accommodate large cations such as K^+ and Ba^{2+}. α-MnO_2 crystallizes either in the tetragonal space group $I\,4/m$ or the monoclinic $C\,2/m$, which is a subgroup of the former, with unit cell parameters $a \approx 10$Å, $c = 2.8$Å on the tetragonal basis.[44]

The hydrothermal synthesis for production of α-MnO_2 studied here is represented by reaction (4).[55]

$$(4) \quad 3MnSO_{4(aq)} + 2KMnO_{4(aq)} + 2H_2O_{(l)} \xrightarrow{\Delta} 5MnO_{2(s)} + 2H_2SO_{4(aq)} + K_2SO_{4(aq)}$$

The precursor used here was prepared by dissolving $KMnO_4$ in water to a Mn^{7+} concentration of 0.4 M and then adding the appropriate mass of $MnSO_4$ to obtain a Mn^{2+} concentration of 0.6 M. Note that the results discussed here are from precisely this method of precursor preparation since it was found that if the precursor chemicals were mixed in a different order the reaction produced different quantitative and qualitative results. Dependency upon the order of chemical mixing for hydrothermal *in situ* studies has been observed previously.[27]

2.2.1.4 *δ-MnO_2*

The δ-MnO_2 structure is a layered structure consisting of edge sharing MnO_6 octahedra that bond to form MnO_2 sheets (see Figure 7d). Between these sheets different kinds of ions and/or solvent molecules reside. In the ordered state the sheets stack along the crystallographic [001] direction in an ordered manner. The chemical species between the layers are also ordered. The interlayer spacing depends upon the type of species that are present between the layers. The ordered δ-MnO_2 crystallizes in the trigonal space group $R\bar{3}m$ with approximate unit cell parameters $a \approx 2.85$ Å, $c \approx 20$ Å, which are dependent upon the exact oxidation state of manganese and the nature of the interlayer species. δ-MnO_2 exhibits varying degrees of disorder, which is evident from the PXRD patterns. The smallest degree of disorder is random positioning of the species in between the layers. It is also possible for the MnO_2 layers to be mismatched but remain parallel; this means reflections with mixed miller indexes containing an / component disappear. Finally, the most disordered state is when the MnO_2 layers are nonparallel meaning Bragg reflections containing an /component in their miller index become diffuse or disappear.[44]

The hydrothermal synthesis of δ-MnO_2 was achieved by heating $KMnO_4$ dissolved in HCl according to reaction (5).

$$(5) \quad 2KMnO_{4(aq)} + 8HCl_{(aq)} \xrightarrow{\Delta} 2MnO_{2(s)} + 3Cl_{2(g)} + 4H_2O_{(l)} + 2KCl_{(aq)}$$

The precursor solution used here was prepared by dissolving $KMnO_4$ in 2.0 M HCl to a Mn^{7+} concentration of 0.8 M.

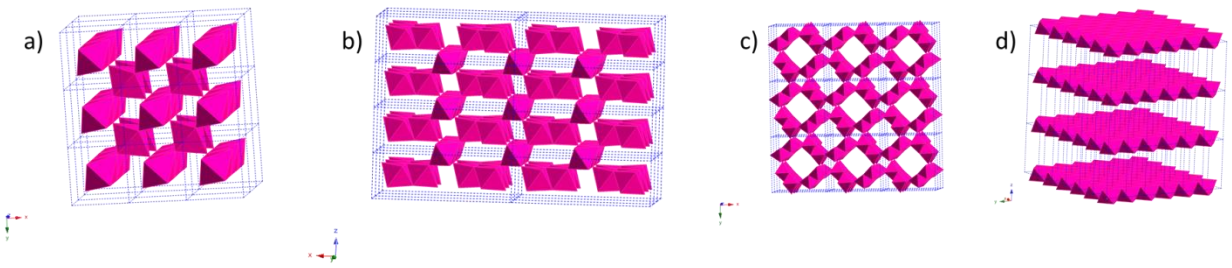

Figure 7: Graphical representation of the crystal structures of different MnO_2 phases using MnO_6 octahedra. a) β-MnO_2 b) γ-MnO_2 c) α-MnO_2 d) δ-MnO_2.

2.2.2 *In situ* PXRD and PDF characterization

The *in situ* data discussed here was collected at two separate beam times. The total scattering data was collected at beamline P02.1 PETRA-III at DESY in Hamburg, Germany in August-September 2013. The PXRD data was collected at beamline I711MAX II at MAX-lab in Lund, Sweden in December 2013. All experiments were performed at constant pressure, 250 bar, and isothermal reaction conditions with varying set point temperature. Table 2 presents an overview of the reaction conditions data was collected.

Table 2: Overview of the *in situ* data collected for the four different solvothermal syntheses at different reaction conditions

SPT [°C]	β	γ	α	δ
100		PDF	PDF	
150			PDF (failed)	
200	PDF	PDF	PDF/PXRD	PDF/PXRD
225			PXRD	
250		PDF	PDF/PXRD	PDF
275			PXRD	
300	PDF/PXRD	PDF	PDF/PXRD	PDF
350	PDF			PDF
400	PDF/PXRD			
450	PDF/PXRD			PXRD

The *in situ* measurements for γ- and δ-MnO_2 did not result in data of sufficient quality and therefore these two systems will not be discussed further in this report. On the other hand, both β- and α-MnO_2 syntheses provided some very interesting results.

2.2.2.1 β-*MnO_2*

PXRD patterns of the β-MnO_2 precursor solution prior to heating showed no Bragg peaks indicating no crystalline order. The lack of crystalline order is to be expected from the clear solution of dissolved $Mn(NO_3)_2$. The PDF from the same solution reveals local order in the solution, see Figure 8. Two definite bond lengths are observed. One at r≈1.2Å agreeing well with the N-O bond length in the nitrate ion,[5] and another at r≈2.2 Å fitting well to the Mn-O bonding length in a hydrated Mn^{2+} complex.[57] This shows that the $Mn(NO_3)_2$ was fully dissolved and no further reaction takes place before heating.

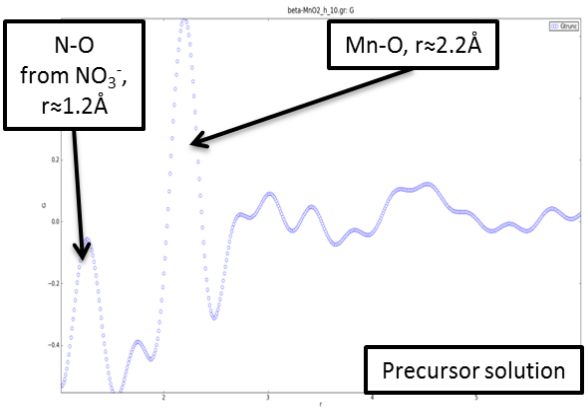

Figure 8: PDF of β-MnO_2 precursor solution.

The results from the *in situ* measurements can be divided into three scenarios, i.e. if the reaction conditions are subcritial (T<374°C), near critical (T≈374°C) or supercritical (T>374°C). At subcritical conditions the PXRD data shows no significant change and no Bragg peaks appear meaning that no crystalline material forms at subcritical conditions. The PDF data confirms that the solution

remains unchanged at these conditions since the PDF obtained after 30 minutes at SPT=300°C is identical to the precursor solution.

At near critical conditions (SPT=400°C, RealT≈360°C) the PXRD data shows rapid formation of β-MnO_2 nanocrystallites that grow insignificantly after the first 30 seconds of reaction. The best Rieveld fit to the data is obtained by assuming rod shaped crystallites[19] with the rod axis along the crystallographic [001] direction. Focusing on the PDF data collected after the heating is initiated, peaks that can be refined using the β-MnO_2 phase (Figure 9a) are observed. Interestingly the large peak at r≈2.2 Å, observed at the same position in the precursor solution, does not disappear after heating is initiated and stays throughout the complete analyzed reaction time (25 minutes). Combination of the information gained from the PXRD and PDF datasets reveals that at near critical reaction conditions crystalline nanorods are formed directly from the precursor complex. It is further seen that the yield of the reaction is relatively low since a lot of the precursor complex is still present after prolonged reaction time.

At supercritical reaction conditions, large β-MnO_2 crystallites form quickly within 30 seconds. The formation rate then slows down significantly. This is observed in the time resolved PXRD data presented in Figure 9c. After approximately 7 minutes of reaction, a sudden increase in the scale factor of the PXRD indicates rapid formation of more β-MnO_2 crystallites followed again by a period of slower formation rate until the reaction is stopped. Initially I believed the observed increase in scale factor was because of instrumental instability but the rapid increase was confirmed by reproducing the experiment during a different beamtime at the same beamline 7 months later. The PDF data confirms that large β-MnO_2 crystals are formed initially, see Figure 9b. Close inspection of the PDF at r≈2.2 Å reveals there is still precursor complex in the solution. Unfortunately the PDF measurements did not run for the time needed to observe the large scale factor increase that would hopefully confirm further β-MnO_2 crystallite formation and subsequent diminishing of the amount of precursor complex in solution. Combining these results shows that β-MnO_2 crystallites form in two rapid formation steps. The yield of the reaction is low after the first step but increases significantly after the second step, although the yield is not 100% even after 25 minutes of reaction.

From the data presented it is seen that where a crystalline phase is formed, this phase is β-MnO_2 and it forms directly from the precursor complex at all reaction conditions. No intermediate steps are observed and there is no obvious reason why the β-MnO_2 phase should be formed rather than any of the other possible phases. Despite this, a lot of practical information about optimal synthesis parameters and crystallite size control has been obtained.

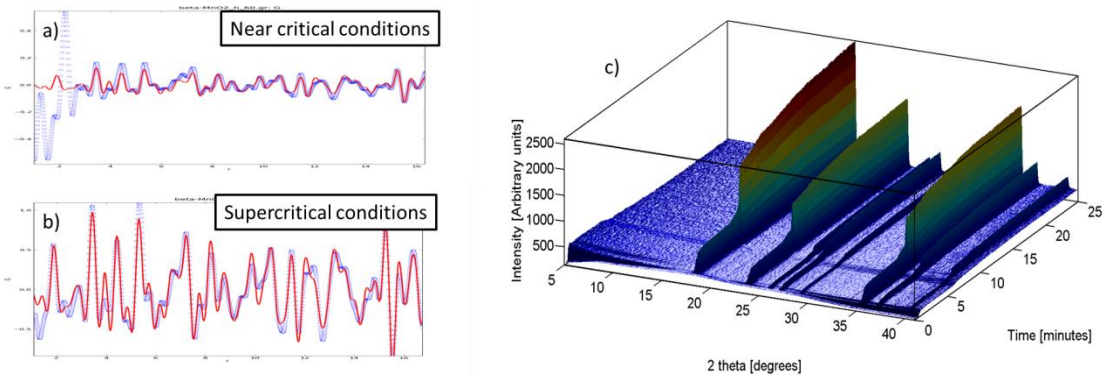

Figure 9: PDF data (blue dots) and refined fit using β-MnO_2 (red line). a) Near critical reaction conditions. b) Supercritical reaction conditions. c) Time resolved PXRD data at supercritical reaction conditions.

2.2.2.2 *α-MnO_2*

In situ PXRD investigations show that the α-MnO_2 reaction can be divided into three stages, see Figure 10a. In stage one, shortly after heating is initiated, α-MnO_2 nanoparticles are formed. After some time, stage two of the reaction sets in where a clear phase transformation from α- to β-MnO_2 is observed. In stage three of the reaction, α-MnO_2 has been completely transformed to β-MnO_2. Looking at the Rietveld refined weight fraction of α-MnO_2, see Figure 10b, it is seen that stage two of the reaction begins earlier at higher temperatures. At 200°C, only stage one is observed within the reaction time measured. Figure 10b also illustrates the slow transformation of α-MnO_2 to β-MnO_2 throughout stage one, giving a mixture of phases upon heating. This indicates that α-MnO_2 is unstable under the given reaction conditions and transforms completely to β-MnO_2 after prolonged reaction time. It is apparent from the data shown here that the transformation happens faster at higher temperatures. However, preliminary results from a reproducibility study of this system conducted at I711 MAX II at MAX-lab in December 2014 show that the onset of stage two, and therefore rate of transformation, varies from experiment to experiment even when running with the same temperature. This indicates that inhomogeneity in the reaction system affects the onset of reaction stage two. Focusing on the PXRD patterns of the precursor solution obtained before heating is initiated, see Figure 10c, two Bragg peaks at 2θ≈7° and 24° are clearly observed on a large background. Both peaks can be indexed to δ-MnO_2. The peak at 2θ≈7° comes from crystalline order between different layers in the structure. It is relatively weak and broad indicating a low degree of ordering in the δ-MnO_2 crystallites formed at room temperature. The limited number and weak intensity of the Bragg peaks for δ-MnO_2 combined with very high background made Rietveld refinements of these data impossible. Therefore no quantitative information is extracted for the precursor solution.

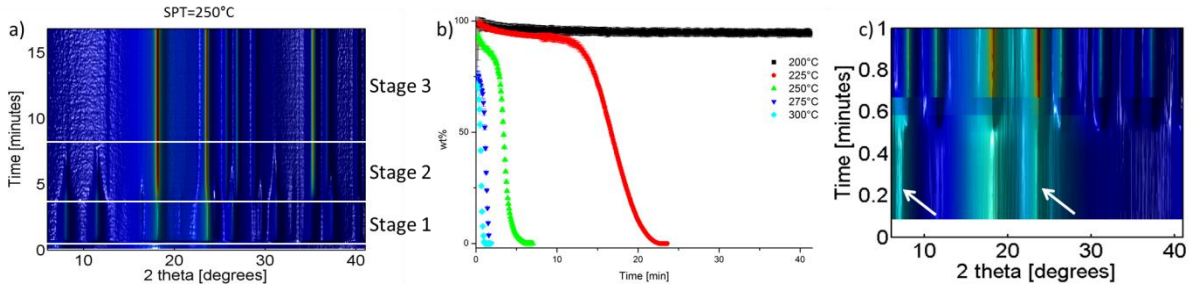

Figure 10: a) Time resolved PXRD data at 250°C showing the three reaction stages. b) wt% of α-MnO_2, refined from PXRD data, (rest is β-MnO_2) as a function of reaction time at different set point temperatures. c) Zoom in of first minute of data acquisition at 250°C marking δ-MnO_2 reflections with white arrows.

By Rietveld refinement of the PXRD data obtained after heating is initiated it is possible, to extract information about the crystallite growth as a function of reaction time. The best fit to the data is obtained by assuming platelet/needle shaped crystallites[19] with the principle axis along the crystallographic [001] direction for both the α- and β-MnO_2 crystallites. The Rietveld refinements show that both the α- and β-MnO_2 form rod-like nanocrystallites with aspect ratios ranging from three to five. A typical growth curve is presented in Figure 11a, which shows that the α-MnO_2 crystallites grow both along the axis and in diameter in stage one and two of the reaction. The β-MnO_2 crystallites seem to form with a certain length in stage two that does not change (within the esd) for the rest of the reaction. The diameter of the β-MnO_2 crystallites increases slightly in stage two before crystallite growth slows down and almost stops in stage three. Crystallite volume as a

function of reaction temperature for the different temperatures used is presented for α-MnO_2 in Figure 11b and for β-MnO_2 in Figure 11c. Interestingly the α-MnO_2 crystallites grow in size even though they are disappearing from the reaction solution. In fact the crystallite growth rate is largest in stage two when the transformation rate of α-MnO_2 → β-MnO_2 is largest. A possible explanation for this behavior is that the smallest α-MnO_2 crystallites are transformed first to β-MnO_2 with subsequent transformation of larger crystallites. This would suggest that the volume average crystallite size increases even though the amount of crystallites decreases. Another interesting trend is that lower reaction temperatures give larger crystallites. This might be explained by fact that at lower temperatures stage one is prolonged giving the α-MnO_2 crystallites longer time to grow bigger. The volume averaged β-MnO_2 crystallite size starts out small and grows fast in stage two. This supports the hypothesis given here that small α-MnO_2 crystallites transform first, with subsequent transformation of larger crystallites. The final crystallite volume of the β-MnO_2 crystallites decreases with increasing temperature with the exception that at SPT=300°C larger crystallites are observed. The trend of decreasing crystallite size could again be explained by longer reaction times at lower temperatures but the explanation for the exception to this trend at 300°C is not obvious. Recently, suspicion arose that the reason for the trend break might have something to do with a mistake in the integration of the 2D diffraction data, but this remains to be confirmed.

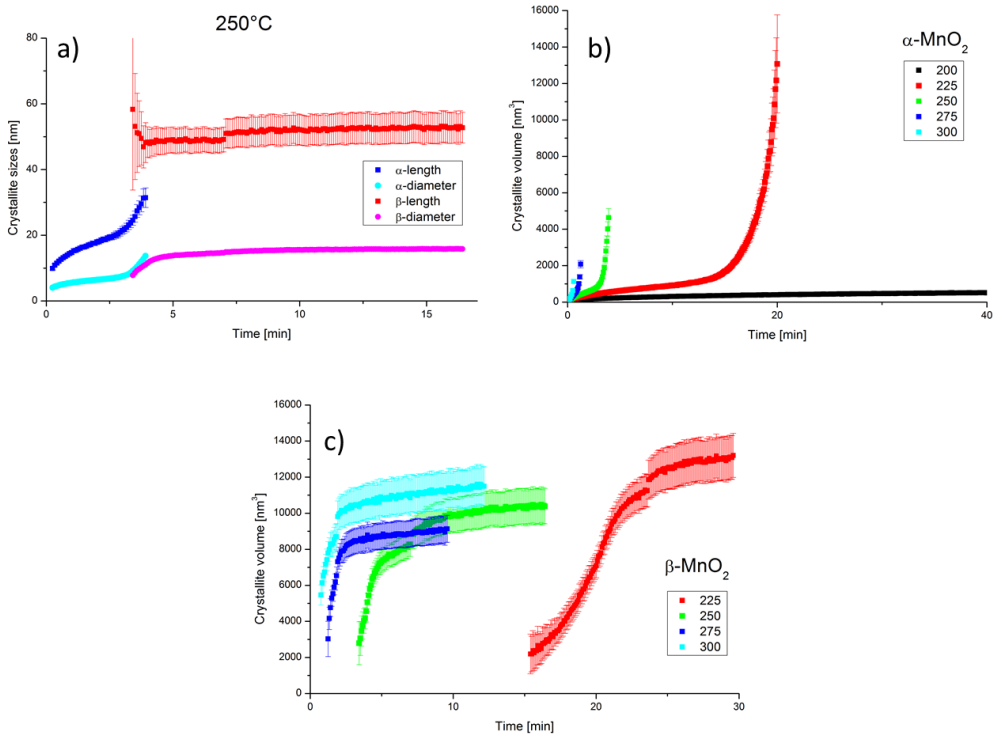

Figure 11: a) Typical growth curves for α- and β-MnO_2, data from STP=250°C. b) Crystallite volume of α-MnO_2 as a function of reaction time. c) Crystallite volume of β-MnO_2 as a function of reaction time.

To understand the reaction mechanism in more detail it is very informative to analyze PDF obtained from *in situ* TS data at three points in the reaction, i.e. the unreacted precursor solution, at stage one and at stage three.

PDF of the precursor solution plotted from r=1-10Å is presented in Figure 12a. Note that peak at r≈1.4 Å is due to the S-O bond in SO_4^- which is present in high concentration in the reaction solution at all reaction stages. It is necessary to include this species in the model used when fitting the data. The way the sulfate group was included in this work is simply done by including the K_2SO_4 phase using a very small coherence length and only refining the scale factor for that particular phase. It is found, as would be expected, that the scale factor of K_2SO_4 is approximately the same throughout the reaction. The best fit is obtained by including both δ- and α-MnO_2 in the model. The coherence length of the phases are refined and found to be ~15 Å and ~2.5 Å for δ- and α-MnO_2, respectively. A coherence length of 2.5 Å for the α-MnO_2 phase is very small and indicates a lack of order extending further than the MnO_6 octahedra that are the basic building unit of all the MnO_2 phases. This means that the precursor solution contains amorphous MnO_2 together with nanodomains, ~1,5 nm in diameter, with sheet like structure similar to δ-MnO_2, see Figure 12b.

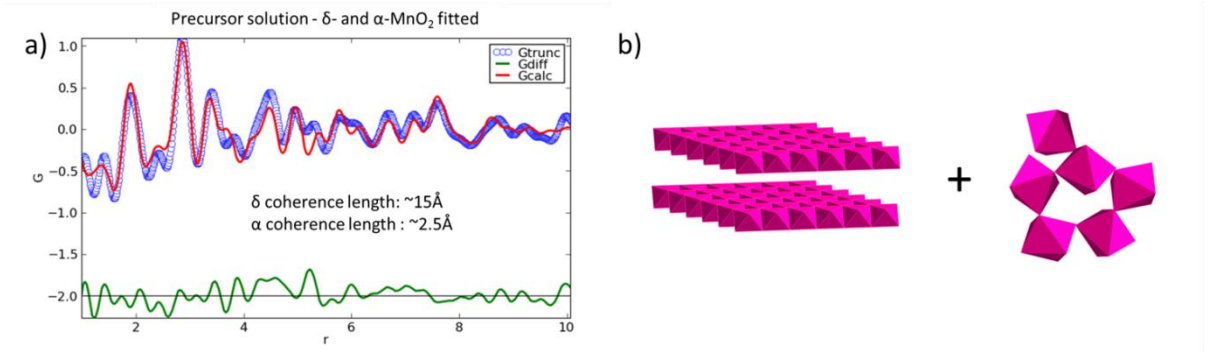

Figure 12: a) PDF of precursor solution (blue dots) with δ- and α-MnO_2 phases fitted (red line). b) Schematic figure of structures present in the precursor solution.

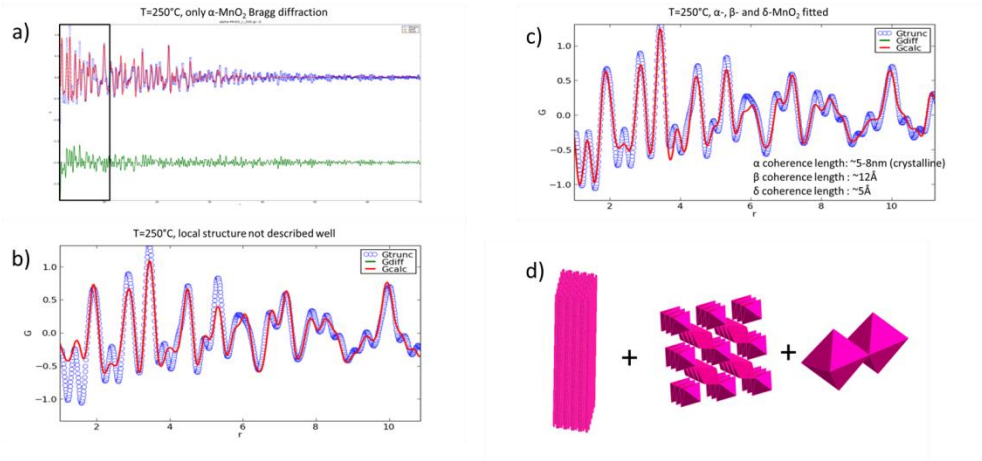

Figure 13: a) PDF of reaction solution in stage 1 fitted to the α-MnO_2 phase. b) Zoom in to boxed area in a) showing fit is not good at low r. c) Better fit obtained by including β- and δ-MnO_2 phases. d) Schematic figure of structures present in stage 1.

Figure 13a shows the PDF of the reaction solution in stage 1 of the reaction. The long range order (r=10-70 Å) is well fitted with the α-MnO_2 phase therefore confirming the PXRD measurements in the same stage. Focusing on the low r region, see Figure 13b, it is observed that a poor fit is obtained here. From this it is clear that some additional short range order is present in the reaction solution at stage 1. The best fit is obtained by including β- and δ-MnO_2 with short coherence

lengths. The refined coherence lengths are ~50-80 Å, ~12 Å and ~5 Å for α-, β- and δ-MnO_2, respectively. The large coherence length of α-MnO_2 is consistent with the fact that Bragg diffraction is observed for this phase. Due to software restrictions, only spherical particle shapes can be fitted, meaning that the refined coherence length of the crystalline α-MnO_2 (and later β-MnO_2) is not representative for this system. Interestingly the refined coherence length from the PDF roughly matches the refined crystallite diameter from the Rietveld refinements of the PXRD data confirming the order of magnitude of the crystallite coherence length. The 5 Å coherence length of the fitted δ-MnO_2 indicates the presence of amorphous material in the reaction solution. The increased coherence length compared to the precursor solution indicates that the smallest units in the amorphous material are probably dimers of edge sharing MnO_6 octahedra. Combining all this information, see Figure 13d, it is seen that at reaction stage one the reaction solution contains crystalline α-MnO_2 nanorods, nanodomains of β-MnO_2 with diameter of ~1.2 nm and amorphous material with increased local ordering compared to the precursor solution.

PDF obtained at reaction stage three is presented in Figure 14a. The high r-region (r=10-70Å) is well fitted with the β-MnO_2 phase confirming the *in situ* PXRD results. By zooming in to the low r-region, see Figure 14b, it is clear that there is additional short range order not described by the β-MnO_2 crystallites. A better fit is obtained by including a short range ordered α-MnO_2 phase. The refined coherence lengths are ~100 Å and ~12 Å for β- and α-MnO_2, respectively, meaning the reaction solution at stage three contains crystalline β-MnO_2 nanorods and α-MnO_2-like nanodomains with a diameter of 1.2 nm. The order of magnitude of the nanorod diameter refined from the PXRD data is confirmed because the coherence length refined from the PDF data is approximately the same.

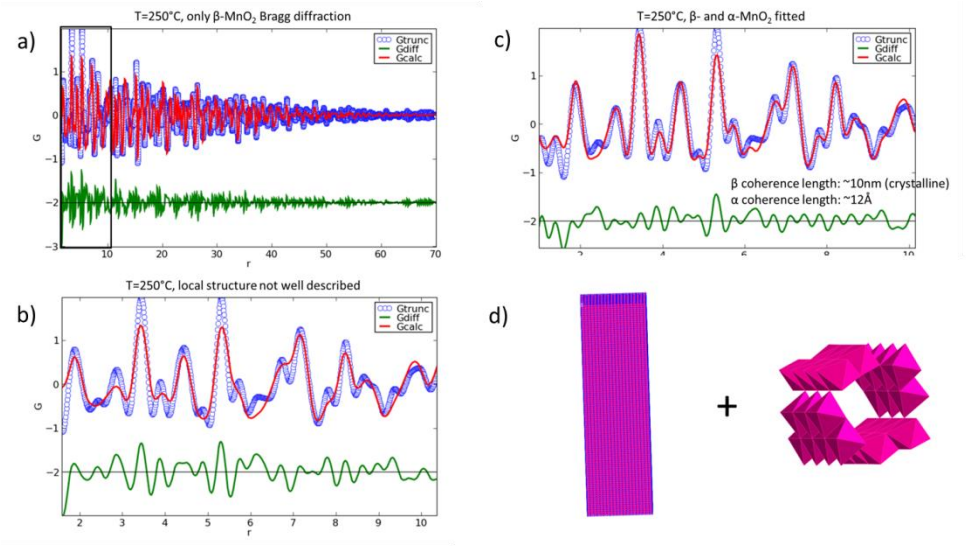

Figure 14: a) PDF of reaction solution in stage 3 fitted to the β-MnO_2 phase. b) Zoom in to boxed area in a) showing fit is not good at low r. c) Better fit obtained by including α-MnO_2 phases. d) Schematic figure of structures present in stage 3.

The presence of amorphous material and β-MnO2 nanodaomins in reaction stage one and α-MnO_2 nanodomains in reaction stage three indicate that the reaction solution never contains phase pure α- or β-MnO_2. If the nanodomains are free in the solution and not incorporated into the crystallites of the crystalline phase it might be possible to produce phase pure samples via washing

after the reaction has been stopped. The answer to whether the nanodomains are incorporated into the structure or free in the solution can be answered by *ex situ* experiment. I.e. stopping the reaction in stage one and stage three, washing the product with water and analyzing the dry powder PDF. This has already been attempted but the experiment failed due to wrong mixing of the precursor solution. Therefore further *ex situ* experiment will have to be conducted.

Figure 15a shows a plot the coherence length refined from the PDF data as a function of reaction time for SPT=250°C, and the different stages of the reaction are clearly visible. When stage two starts, β-MnO_2 domains start growing rapidly and stage three starts when α-MnO_2 domains stop shrinking and amorphous material is no longer observed. Compiling the information gained from the combined *in situ* PXRD and PDF study a possible reaction mechanism can be proposed. At room temperature Mn^{7+} is reduced by Mn^{2+} to give Mn^{4+} in MnO_2. As a result of the low temperature used and the high reaction rate, MnO_2 is not able to form a well ordered crystalline structure instead forming amorphous MnO_2 and nanodomains of relatively disordered δ-MnO_2. When the reaction is initiated by heating, the precursor structures transform to α-MnO_2 crystallites that grow rapidly at first and then slowly. At the same time β-MnO_2 nanodomains are formed that do not grow significantly during stage one. In stage one not all of the amorphous material is incorporated into ordered structures but the local ordering is increased. In stage two transformation of α- to β-MnO_2 is observed. Throughout stage two the β-MnO_2 nanodamains grow rapidly. Early in stage two the α-MnO_2 crystallites keep growing until the α- and β-MnO_2 crystallites are equally big. Then the α-MnO_2 crystallites start shrinking indicating the smallest α-crystallites are the first ones to transform followed by larger crystallites. In stage two the rest of the amorphous material is incorporated into the ordered crystal structures and in the beginning of stage three no amorphous material is observed. Stage three is essentially the end of the reaction since no further transformation occurs. The final product is crystalline β-MnO_2 nanorods and nanodomains with α-MnO_2 like structure. The proposed reaction mechanism does not answer the question why α-MnO_2 is formed in this reaction system but the reason for it transforming to β-MnO_2 can be postulated. The data shows β-MnO_2 nanodomains are formed in the beginning of reaction giving the nucleation sites needed for the phase transformation.

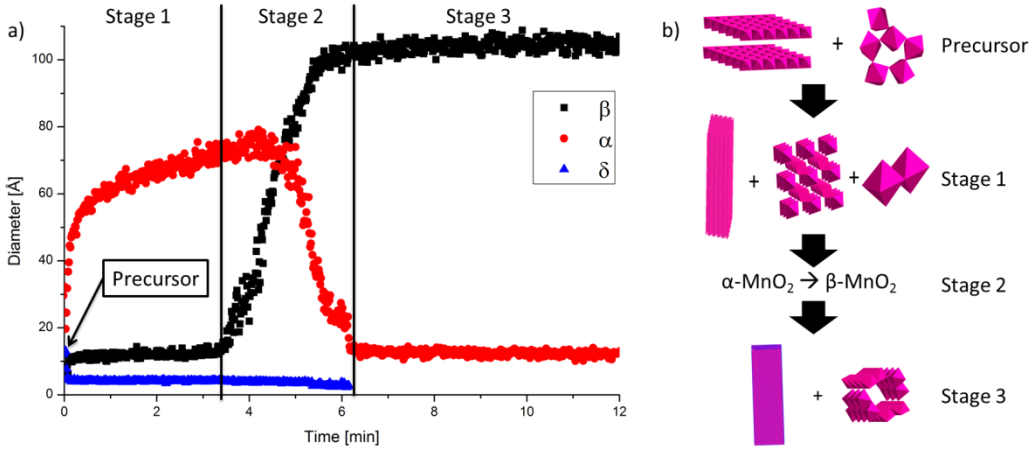

Figure 15: a) Real space refined coherence lengths of α-, β-, and δ-MnO_2 as a function of reaction time at SPT=250°C. b) Proposed reaction mechanism.

3 Outlook

In the last 2 years of PhD studies I will continue researching Li- and Na-ion electrode materials. However I will focus more on examining the relationship between structural properties and battery properties. Moving on from the *in situ* characterization of structural properties that are then inferred to battery properties I will synthesize new types of electrode materials and test battery properties in half cells. In future work, my expertise in *in situ* characterization of solvothermal reactions will primarily be used to control structural properties through synthesis.

The project on the horizon now is synthesis and characterization of layered sodium transition metal oxide materials as described in details below. Without a doubt some new and interesting research topics will emerge in the next 2 years which I will pursue in co-operation with the great research group I am a part of.

3.1 Layered Sodium Transition metal oxides

Layered sodium transition metal oxides have the general chemical formula Na_xMO_2, where x is normally in the range 0.5-1.0 and M represents the transition metal, either pure, bimetallic or trimetallic mixture. These materials crystallize in a layered structure where sodium ions are sandwiched between sheets of edge sharing MO_6 octahedra. Even though all these materials share this basic structural motive, subtle variations in oxygen packing and sodium (and sometimes transition metal) ordering creates a range of crystalline phases with unique crystal structures. The two most common phases are the P2 and O3, where sodium ions are in a prismatic and octahedral site, respectively. Both the P2 and O3 phases can be used as cathode materials for SIB but generally P2 is considered to be a better electrode material due to high sodium ion diffusion rate and restricted slab gliding.[52]

This study will focus on synthesizing and characterizing layered sodium transition metal oxides with varying transition metals. Starting with trying to make the solid solutions of bimetallic compositions of Mn-Ni and Mn-Fe, comparisons will be made to previous work in our research group of the Mn-Co solid solution. Later trimetallic compositions will be synthesized, i.e. Mn-Ni-Fe, Mn-Ni-Co, etc. The amount of sodium (i.e. x in Na_xMO_2) will also be varied to study the effect on material properties.

3.1.1 Synthesis

The layered transition metal oxides will be synthesized using a new two-step synthesis method developed by Dr. Yanbin Shen. Preliminary results indicate that some materials synthesized by this method show improved battery performance in comparison to materials synthesized by conventional solid state synthesis. The first step of the synthesis is a co-precipitation by oxalate of divalent transition metals ions. The second step of the synthesis is a solid state reaction where the transition metal oxalate is mixed, ground and pressed together with a sodium ion source, e.g. sodium carbonate, in the desired stoichiometry. The pressed powder is then heated at approximately 900°C for 12 hours. Experiments have already shown that some optimization of reaction temperature and time, for example, is needed in order to get phase pure materials of different elemental composition.

The materials found to have good battery properties will be studied further by also synthesizing them with a conventional solid state synthesis. Those materials will then be characterized in the

same way as the others in order to determine if the good properties are specific to the materials synthesized by the new method.

3.1.2 Characterization

The synthesized materials will be characterized in detail in order to try to relate material properties to battery properties. This will help us to understand what makes a good battery and how to improve the battery properties to fit a specific application. The techniques that I will use will now be summarized briefly.

3.1.2.1 *Battery properties*

Battery properties will be measured by making electrodes from the synthesized materials and assembling half cells. Half cells testing is a standardized way to measure battery properties that originates from the electrode material. It isolates the effects from the electrode material because all the other parts of the cell are kept the same and are designed not to be a limiting factor in the measurement. For example, the counter electrode is the pure alkali metal meaning there is a surplus of alkali metal ions in the system. Different battery properties are then measured galvanostatically. The most relevant battery property is determination of the voltage profile as a function of the charge/discharge capacity which can be used to calculate the energy stored in the electrode material. The voltage profile can also be used to learn more about the different electrochemical processes occurring in the battery and to determine what kind of battery applications the electrode material is suitable for. Another important battery property is rate capability which is determined by measuring the capacity of the half cell as a function of charge/discharge rate. Last but not least, the capacity retention of the electrode material can be measured in order to determine stability of the electrode material while being used and therefore how long your battery will live.

3.1.2.2 *Phase characterization*

The crystalline phases, phase purity and crystallinity of the synthesized materials will be determined by PXRD. This is done to determine what effect the crystal structure has on the battery properties. It is also important to know if any amorphous material and/or impurity phases are present to establish if this has a positive or a negative impact on battery performance. Characterization by total scattering and PDF analysis will also be a powerful tool to investigate whether there is any local ordering in the material that possibly affects battery properties.

3.1.2.3 *Elemental analysis*

The elemental composition of the synthesized materials will be determined by different techniques. This is done to see if the desired stoichiometry of transition metals is actually obtained and to see how much sodium is incorporated into the crystalline material.

Transition metal stoichiometry is conveniently determined by inductively coupled plasma optical emission spectroscopy (ICP-OES). This method measures the concentration of specific metal ions in a solution where the sample has been dissolved. ICP-OES therefore allows determination of the metal stoichiometry of the whole sample, i.e. both crystalline part and amorphous and can therefore not be used to determine the stoichiometry of the crystalline phase unless the sample is 100% crystalline. A drawback of ICP-OES is that it cannot determine sodium concentration in a reliable way; therefore another technique is necessary to determine the sodium composition.

Examples of alternative techniques are atomic absorption spectroscopy and glass electrode both measuring on dissolved samples and therefore determining the sodium content of both the crystalline and the amorphous material. Another method that can measure elemental composition is energy dispersive X-ray spectroscopy (EDX), using an electron microscope. The advantage of this method is that differences in crystalline and amorphous material may be detected by focusing the electron beam on crystalline and amorphous parts separately. The drawback is that EDX only probes a very small part of the sample. Sodium content of the crystalline phase can also be estimated by PXRD, i.e. by refining the sodium site occupancy. This would require high quality PXRD data and good estimations for data corrections, such as X-ray absorption in order to be accurate. Note also that transition metal stoichiometry cannot be determined by PXRD because the scattering power of the different transition metals is so similar.

3.1.2.4 *Size and morphology distribution*

If the synthesized crystallites are found to be nanosized, i.e. small enough to show peak broadening in PXRD, the size and morphology can be analyzed with peak profile analysis and the Scherrer equation. Size distribution and morphology of particles, i.e. not just the crystallites, can be investigated by scanning electron microscope (SEM) and transmission electron microscope (TEM). Information about the size and morphology can be compared to battery performance to see the effect of those parameters.

3.1.2.5 *In operando characterization of working half cells*

An experimental setup using a conventional laboratory diffractometer to collect time resolved PXRD patterns of the electrode material in a wide 2θ range in a working LIB and SIB half cell (*in operando* characterization) has been designed and developed by our research group, see Figure 16.[58] *In operando* characterization gives the opportunity to study structural changes; such as unit cell changes, phase transformation, etc., in the electrode material while it is being charged and discharged. The information can be used to try to understand why the electrode material exhibits certain battery properties; e.g. stability, high capacity, etc., or lack thereof. More practically it can be used to optimize the working conditions for a certain electrode material, e.g. by seeing what conditions trigger irreversible processes.

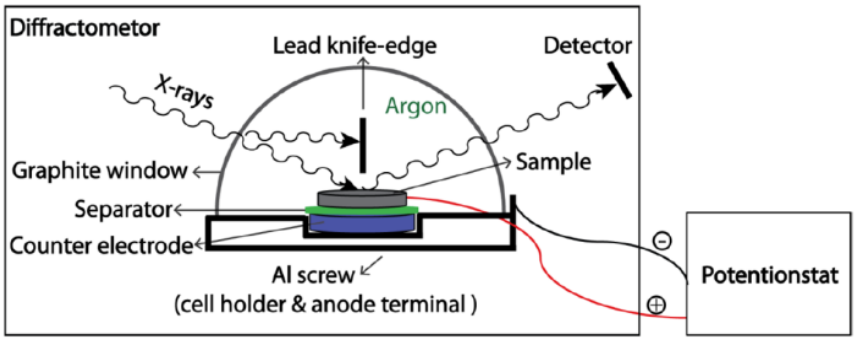

Figure 16: Schematic figure of the *in operando* cell, graphics by Dr. Yanbin Shen

I will use the *in operando* characterization to learn more about the layered sodium transition metal oxide materials and see if the observed battery properties can be understood by structural changes during charge and discharge.

4 References

1. T. N. K. Tozawa, *Progress in Batteries and Solar Cells*, 1990, 9.
2. R. J. Brodd, in *Lithium-Ion Batteries: Science and Technology*, ed. R. J. B. Masaki Yoshio, Akaya Kozawa, Springer, 2009, ch. 1, pp. 1-8.
3. J. B. Goodenough and K.-S. Park, *J. Am. Chem. Soc.*, 2013, 135, 1167-1176.
4. S.-W. Kim, D.-H. Seo, X. Ma, G. Ceder and K. Kang, *Advanced Energy Materials*, 2012, 2, 710-721.
5. C. E. H. A. G. Sharpe, *Inorganic Chemistry*, Pearson Education Limited, Essex, 3 edn., 2008.
6. K. M. Ø. Jensen, M. Christensen, H. P. Gunnlaugsson, N. Lock, E. D. Bøjesen, T. Proffen and B. B. Iversen, *Chemistry of Materials*, 2013, 25, 2282-2290.
7. P. G. Bruce, B. Scrosati and J.-M. Tarascon, *Angew. Chem. Int. Ed.*, 2008, 47, 2930-2946.
8. A. S. Arico, P. Bruce, B. Scrosati, J.-M. Tarascon and W. van Schalkwijk, *Nat Mater*, 2005, 4, 366-377.
9. Y. S. Hu, L. Kienle, Y. G. Guo and J. Maier, *Advanced Materials*, 2006, 18, 1421-1426.
10. R. I. Walton, *Chemical Society Reviews*, 2002, 31, 230-238.
11. A. Rabenau, *Angewandte Chemie International Edition in English*, 1985, 24, 1026-1040.
12. M. Yoshimura and K. Byrappa, *J Mater Sci*, 2008, 43, 2085-2103.
13. *Acta Crystallographica Section A*, 1992, 48, 922-946.
14. H. L. M. G. Artioli, in *Fundamentals of Crystallography*, ed. C. Giacovazzo, International Union of Crystallography Oxford University Press, 2011, ch. 5, pp. 301-416.
15. C. Giacovazzo, in *Fundamentals of Crystallography*, ed. C. Giacovazzo, International Union of Crystallography Oxford University Press, 2011, ch. 3, pp. 157-234.
16. P. Scardi, in *Powder Diffraction: Theory and Practice*, The Royal Society of Chemistry, 2008, ch. 13, pp. 376-413.
17. R. A. Young, in *The Rietvled method*, ed. R. A. Young, International Union of Crystallography Oxford University Press, 1993, ch. 1, pp. 1-38.
18. J. Rodríguez-Carvajal, *Phys. B*, 1993, 192, 55-69.
19. C. Greaves, *Journal of Applied Crystallography*, 1985, 18, 48-50.
20. M. Jarvinen, *J. Appl. Crystallogr.*, 1993, 26, 525-531.
21. E. Takeshi and S. J. L. Billinge, in *Pergamon Materials Series*, eds. E. Takeshi and J. L. B. Simon, Pergamon, 2012, vol. Volume 16, ch. 1, pp. 1-25.
22. E. Takeshi and S. J. L. Billinge, in *Pergamon Materials Series*, eds. E. Takeshi and J. L. B. Simon, Pergamon, 2012, vol. Volume 16, ch. 3, pp. 55-111.
23. E. Takeshi and S. J. L. Billinge, in *Pergamon Materials Series*, eds. E. Takeshi and J. L. B. Simon, Pergamon, 2012, vol. Volume 16, ch. 6, pp. 259-295.
24. C. L. Farrow, P. Juhas, J. W. Liu, D. Bryndin, E. S. Bozin, J. Bloch, P. Th and S. J. L. Billinge, *Journal of Physics: Condensed Matter*, 2007, 19, 335219.
25. P. Norby, *Curr. Opin. Colloid Interface Sci.*, 2006, 11, 118-125.
26. J. R. Eltzholtz, C. Tyrsted, K. M. O. Jensen, M. Bremholm, M. Christensen, J. Becker-Christensen and B. B. Iversen, *Nanoscale*, 2013, 5, 2372-2378.
27. H. L. Andersen, K. M. Ø. Jensen, C. Tyrsted, E. D. Bøjesen and M. Christensen, *Cryst. Growth Des.*, 2014, 14, 1307-1313.
28. C. Tyrsted, B. R. Pauw, K. M. Ø. Jensen, J. Becker, M. Christensen and B. B. Iversen, *Chemistry – A European Journal*, 2012, 18, 5759-5766.
29. K. M. Ø. Jensen, M. Christensen, C. Tyrsted, M. Bremholm and B. B. Iversen, *Cryst. Growth Des.*, 2011, 11, 753-758.
30. K. M. Ø. Jensen, M. Christensen, P. Juhas, C. Tyrsted, E. D. Bøjesen, N. Lock, S. J. L. Billinge and B. B. Iversen, *J. Am. Chem. Soc.*, 2012, 134, 6785-6792.
31. D. Saha, K. M. Ø. Jensen, C. Tyrsted, E. D. Bøjesen, A. H. Mamakhel, A.-C. Dippel, M. Christensen and B. B. Iversen, *Angew. Chem. Int. Ed.*, 2014, 53, 3667-3670.

32. J. Becker, M. Bremholm, C. Tyrsted, B. Pauw, K. M. O. Jensen, J. Eltzholt, M. Christensen and B. B. Iversen, *J. Appl. Crystallogr.*, 2010, 43, 729-736.
33. Y. Gao and J. R. Dahn, *J. Electrochem. Soc.*, 1996, 143, 100-114.
34. J. Akimoto, Y. Takahashi, Y. Gotoh and S. Mizuta, *Chemistry of Materials*, 2000, 12, 3246-3248.
35. T.-F. Yi, C.-L. Hao, C.-B. Yue, R.-S. Zhu and J. Shu, *Synthetic Metals*, 2009, 159, 1255-1260.
36. B. J. Liddle, S. M. Collins and B. M. Bartlett, *Energ Environ Sci*, 2010, 3, 1339-1346.
37. Y. C. Zhang, H. Wang, H. Y. Xu, B. Wang, H. Yan, A. Ahniyaz and M. Yoshimura, *Solid State Ionics*, 2003, 158, 113-117.
38. K. Sathiyaraj, Gangulibabu, D. Bhuvaneswari and N. Kalaiselvi, *Ionics*, 2011, 17, 49-59.
39. S. H. Ye, J. Y. Lv, X. P. Gao, F. Wu and D. Y. Song, *Electrochimica Acta*, 2004, 49, 1623-1628.
40. X. Hao, O. Gourdon, B. J. Liddle and B. M. Bartlett, *J. Mater. Chem.*, 2012, 22, 1578-1591.
41. K. Numata, in *Lithium-Ion Batteries: Science and Technology*, ed. R. J. B. Masaki Yoshio, Akaya Kozawa, Springer, 2009, ch. 17, pp. 323-328.
42. J. F. von Bülow, H.-L. Zhang and D. E. Morse, *Adv. Energy Mater.*, 2012, 2, 309-315.
43. S. Birgisson, K. M. O. Jensen, T. L. Christiansen, J. F. von Bulow and B. B. Iversen, *Dalton Transactions*, 2014, 43, 15075-15084.
44. J. H. Albering, in *Handbook of Battery Materials*, ed. J. O. Besenhard, Wiley - VCH, Weinheirn ; New York ; Chichester ; Brisbane ; Singapore ; Toronto, 1999, ch. 2-1, pp. 85-112.
45. V. B. J. G. H. R. R. Tellgren, *Am. Mineral.*, 1998, 83, 786-793.
46. B. B. Laird, *University Chemistry*, McGraw-Hill Higher Education, New York, 2009.
47. Z.-Q. L. Si-Wen Xie; Shuang Chen, Chang-Wei Xu, *International Journal of electrochemical science*, 2011, 6, 882-888.
48. L. Espinal, S. L. Suib and J. F. Rusling, *Journal of the American Chemical Society*, 2004, 126, 7676-7682.
49. M. Winter and R. J. Brodd, *Chemical Reviews*, 2004, 104, 4245-4270.
50. M. Toupin, T. Brousse and D. Bélanger, *Chemistry of Materials*, 2002, 14, 3946-3952.
51. M. M. Thackeray, *Progress in Solid State Chemistry*, 1997, 25, 1-71.
52. V. Palomares, M. Casas-Cabanas, E. Castillo-Martinez, M. H. Han and T. Rojo, *Energ Environ Sci*, 2013, 6, 2312-2337.
53. W. Wei, X. Cui, W. Chen and D. G. Ivey, *Chemical Society Reviews*, 2011, 40, 1697-1721.
54. W. H. Baur, *Acta Crystallographica Section B*, 1976, 32, 2200-2204.
55. F. Cheng, J. Zhao, W. Song, C. Li, H. Ma, J. Chen and P. Shen, *Inorganic Chemistry*, 2006, 45, 2038-2044.
56. L. I. Hill and A. Verbaere, *Journal of Solid State Chemistry*, 2004, 177, 4706-4723.
57. D. D. Petrovic, S.; Krstanovic, I., *Zeitschrift fuer Kristallographie, Kristallgeometrie, Kristallphysik, Kristallchemie*, 1976, 144, 334-340.
58. Y. Shen, E. E. Pedersen, M. Christensen and B. B. Iversen, *Review of Scientific Instruments*, 2014, 85, 104103-104103-104106.

Steinar Birgisson, Synthesis and characterization of Li- and Na-ion battery materials, 2015

Department of Engineering
Aarhus University
Edison, Finlandsgade 22
8200 Aarhus N
Denmark

Tel.: +45 4189 3000